Supplementary Information (SI) for Journal of Materials Chemistry A.

Supplementary Information

High Proton Conductivity of H_xWO_3 at Intermediate Temperatures: Unlocking Its Application as a Mixed Ionic–Electronic Conductor

Rantaro Matsuo[1], Tomoyuki Yamasaki[1,*], and Takahisa Omata[1,*]

[1] Institute of Multidisciplinary Research for Advanced Materials (IMRAM),
Tohoku University, 2-1-1 Katahira, Aoba-ku, Sendai 980-8577, Japan.

S1. Microstructure of sintered H_xWO_3

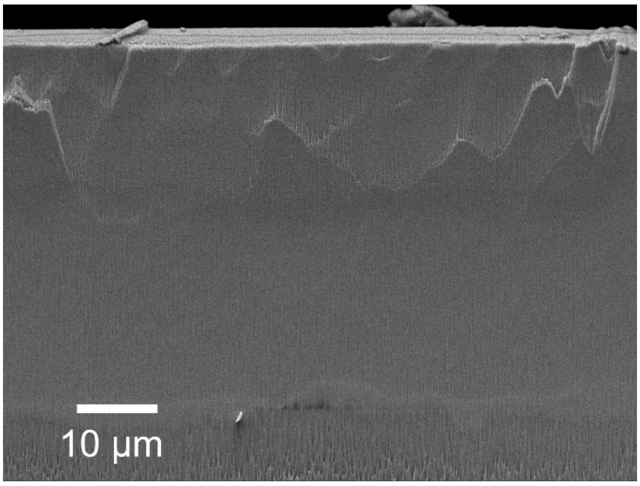

Figure S1. Cross-sectional SEM image of H_xWO_3. The cross-sectional surface was prepared using a cross-section polisher after cutting the hydrogenated WO_3 pellet. Needle-like features were observed on the cross-sectional surface as a result of ion-beam polishing. Grain boundaries were too fine to be resolved, suggesting a compact and homogeneous microstructure composed of very fine crystallites.

S2. Hydrogen distribution in the sintered H_xWO_3 measured by TOF-SIMS

S2.1. Background measurement of hydrogen in WO_3

To evaluate the background hydrogen signal in the TOF-SIMS analysis and determine the necessary sputtering time required to eliminate surface contamination, depth profile measurements were conducted on a reference WO_3 sintered pellet (annealed in flowing oxygen at 800 °C for 10 h) as well as on the H_xWO_3 pellet. The TOF-SIMS depth profiles of the secondary ions were acquired in the negative polarity mode using a Bi^+ primary ion beam (25 kV, 1.0 pA) and a Cs^+ sputter ion beam (2 kV, 145 nA). Figure S2(a) shows the depth profiles of H^- and OH^- signals, normalized to the W^- signal for reference WO_3 and H_xWO_3 pellets. In the reference WO_3 sample, the signals gradually decayed toward the interior of the pellet and became nearly constant after approximately 60 min of sputtering, indicating the elimination of the contribution from surface-adsorbed species. In contrast, for the H_xWO_3 sample, the intensities of H^- and OH^- signals remained nearly constant throughout the sputtering process. Even after sputtering beyond the depth at which surface contributions were no longer observed in the reference WO_3 sample, the signal intensities in H_xWO_3 remained approximately an order of magnitude higher than those in the reference. These results clearly demonstrate that hydrogen in the H_xWO_3 sample can be reliably detected above the background level observed in the reference WO_3 sample.

S.2.2. SIMS area imaging of the cross-section of H_xWO_3

To obtain SIMS imaging data free from surface contamination, a thin surface layer was sputtered prior to acquisition, and imaging was initiated from the depth at which the signal intensities of H^- and OH^- became stable. The imaging area was selected 300 μm inward from the edge of the pellet. A 500 × 500 μm^2 region was imaged to visualize the lateral distribution of hydrogen. Figure S2(b) displays lateral SIMS images of H^-, OH^-, and W^-. In these images, the left edge corresponds to a depth of 300 μm from the surface, and the right edge corresponds to approximately 800 μm. To convert the SIMS images into a concentration profile along the thickness direction of the sintered pellet (Figure 1 (b)), the signal intensities were integrated along the Y-direction.

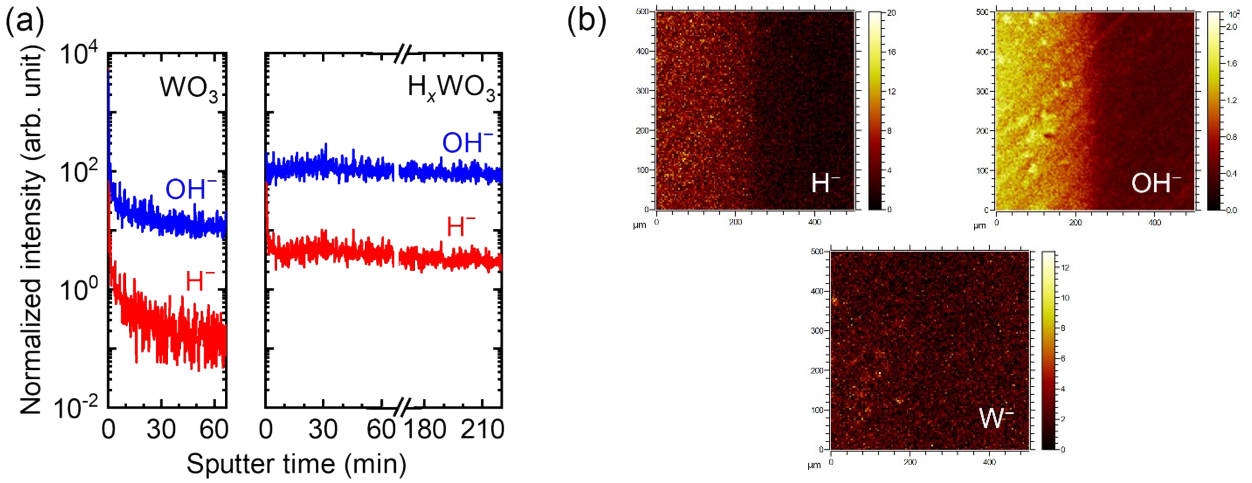

Figure S2. (a) Depth profiles of H^- and OH^- signals normalized to the W^- signal for reference WO_3 and H_xWO_3 pellets. (b) Lateral SIMS images of H^-, OH^-, and W^- in the vicinity of the phase boundary in H_xWO_3.

S3. Quantification of hydrogen in sintered H_xWO_3 by TDS

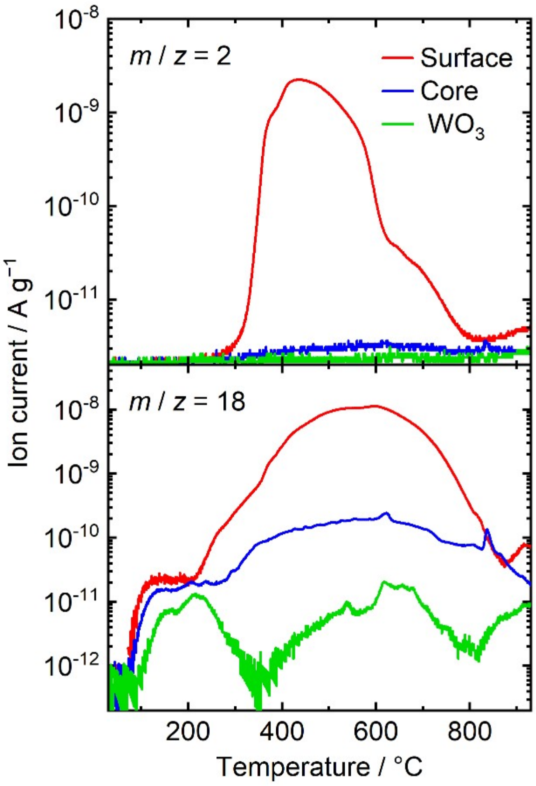

Figure S3. TDS curves of *m*/*z* = 2 (H_2) and 18 (H_2O) for the hydrogen-rich surface (red) and hydrogen-poor core (blue) regions of H_xWO_3 along with WO_3 pellet annealed in oxygen at 800 °C as a reference (green). The release of hydrogen from H_xWO_3 in the form of not only H_2 but also H_2O is likely due to heating under vacuum conditions.

Table S1. Summary of the quantification of hydrogen released as H_2 and H_2O.

	Surface	Core
H released as H_2 / cm^{-3}	1.3×10^{21}	3.2×10^{17}
H released as H_2O / cm^{-3}	3.2×10^{21}	8.9×10^{19}
Total H / cm^{-3}	4.5×10^{21}	8.9×10^{19}
x in H_xWO_3	0.24	0.0048

S4. Growth behavior of the hydrogen-rich region by hydrogen annealing

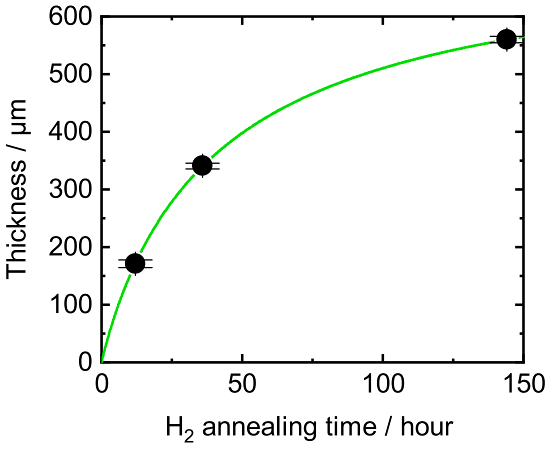

Figure S4. Thickness variation of the hydrogen-rich region as a function of annealing time. The green curve represents a fitting result. The sintered WO_3 samples were annealed in a hydrogen atmosphere at 300 °C for varying durations. The thickness of the hydrogen-rich region, measured from the Pd-deposited surface, gradually increases with annealing time.

S5. Supporting details of the electron-blocking measurement

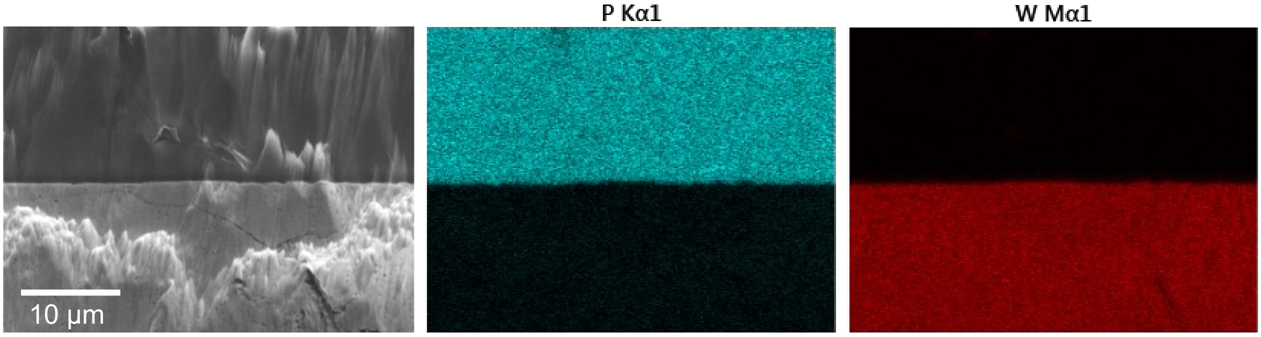

Figure S5. Cross-sectional SEM image of the electron-blocking cell and the corresponding elemental maps for P Kα and W Mα obtained by energy-dispersive X-ray spectroscopy (EDX). The elemental distributions confirm the presence of the phosphate glass electrolyte and the H_xWO_3 layer. No delamination or gap is observed at the interface, indicating that the phosphate glass and H_xWO_3 are well adhered.

S5.1. Considerations of interfacial contributions in the electron-blocking cell

To clarify the possible effects of interfacial resistances in the electron-blocking measurements, we carefully examined the structure of the measurement cell and performed several control experiments. A schematic of the interfaces is shown in Figure S6(a). The interfaces can be summarized as follows:

- **Interface A**: Pd film / H_2 gas
- **Interface B**: Pd film / glass
- **Interface C**: Pd film / H_xWO_3
- **Interface D**: Glass / H_xWO_3
- **Interface E**: Triple-phase boundary of glass, H_xWO_3, and gas phase
- **Interface F**: Boundary between hydrogen-rich and hydrogen-poor regions within H_xWO_3

(i) Interfaces A and B

We prepared a Pd/glass/Pd cell and measured the current response under a DC bias (Figure S6(b). This configuration includes only interfaces A and B. The cell exhibited a much larger steady-state current than the electron-blocking cell, and no pronounced current decay was observed upon voltage application. These results indicate the absence of significant charge accumulation or interfacial polarization, consistent with efficient hydrogen dissociation/recombination at the Pd surface. We therefore conclude that the resistance contributions of interfaces A and B are negligible in the electron-blocking cell.

(ii) Interfaces C, D, and E

We then compared electron-blocking cells with and without a Pd interlayer between the glass and H_xWO_3 (Figure S6(c)). With the Pd interlayer (interface C), the current increased by a factor of ~3 and reached steady state more rapidly, compared with the configuration without Pd (interface D only). This demonstrates that interface C provides an efficient pathway for proton injection from glass into H_xWO_3, whereas interface D alone introduces higher resistance and capacitance. Moreover, the pronounced current enhancement by introducing the Pd interlayer suggests that electronic current from hydrogen redox reactions at interface E contribute only a minor fraction of the total current. Since the Pd interlayer is not in direct contact with the gas phase, electrochemical reactions such as hydrogen evolution or uptake ($2H^+ + 2e^- = H_2$) are unlikely to occur there under the modest overpotentials applied. Therefore, the predominant current observed with the Pd interlayer arises from proton transport through interface C into H_xWO_3.

(iii) Interface F

Finally, interface F, located between hydrogen-rich and hydrogen-poor regions of H_xWO_3, is expected to play a key role in the impedance response. In particular, the markedly lower proton diffusivity in the hydrogen-poor region can account for the diffusion-limited behavior observed at low frequencies. A more detailed discussion of this assignment is provided in the main text.

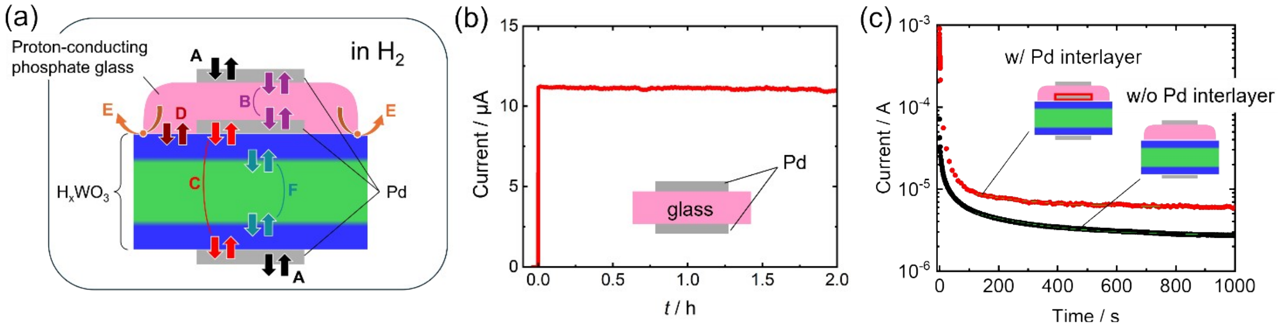

Figure S6. (a) Schematic illustration of the electron-blocking cell, showing the possible interfaces: (A) Pd/hydrogen gas, (B) Pd/glass, (C) Pd/H_xWO_3, (D) glass/H_xWO_3, (E) glass/H_xWO_3/hydrogen gas, and (F) $H_{0.24}WO_3/H_{0.0048}WO_3$. (b) Time evolution of DC current under an applied voltage of 100 mV for a Pd/glass/Pd cell, which includes only interfaces A and B. (c) Comparison of the DC current response under an applied voltage of 100 mV in electron-blocking cells with and without a Pd interlayer at the glass/H_xWO_3 interface.

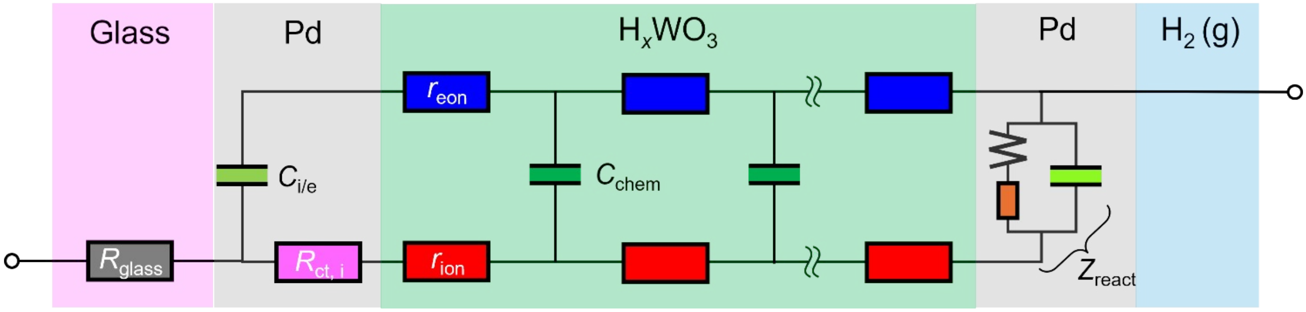

Figure S7. Illustration of the equivalent circuit for the asymmetric electron-blocking cell based on the transmission line model. The model includes ionic and electronic conduction pathways in the H_xWO_3 pellet, as well as charge transfer processes at the glass blocking electrode interface and reactions at the gas–solid interface. The effects of hydrogen distribution inhomogeneity or the presence of multiple phases in H_xWO_3 are not considered.

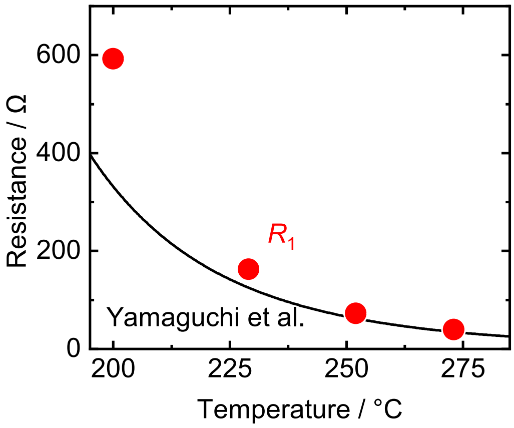

Figure S8. Temperature dependence of R_1 compared with the resistance calculated for the glass with the same geometry using the reported conductivity data[S1].

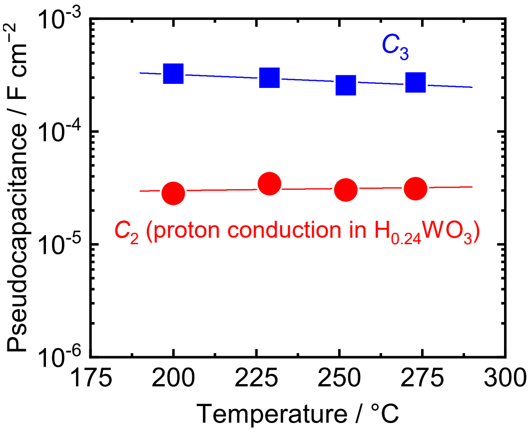

Figure S9. Temperature dependence of the pseudocapacitances corresponding to arc R_2 and arc R_3, obtained from equivalent circuit fitting of the impedance spectra.

S6. Electronic conductivity of H_xWO_3

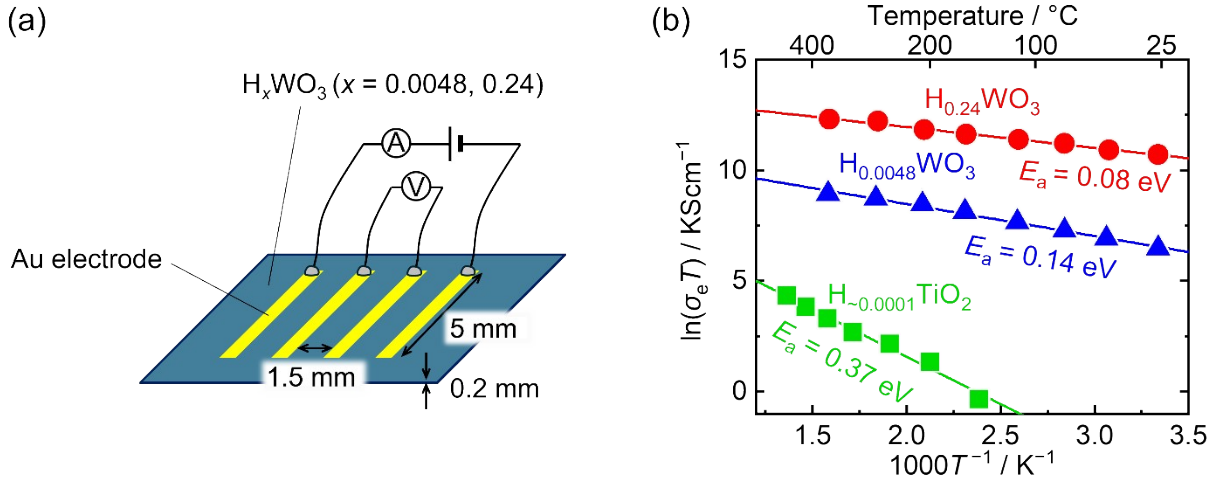

Figure S10. (a) Illustration of the planar sample for electronic conductivity measurements using the four-probe method. (b) Arrhenius plots of the electronic conductivity for $H_{0.24}WO_3$ (red circle), $H_{0.0048}WO_3$ (blue triangle), and $H_{\sim 0.0001}TiO_2$ (green square) with the corresponding activation energies[S2]. The electronic conductivities of $H_{0.24}WO_3$ and $H_{0.0048}WO_3$ were measured under Ar to prevent changes in hydrogen content, while that of $H_{\sim 0.0001}TiO_2$ was measured under H_2 atmosphere.

REFERENCES

S1 T. Yamaguchi, S. Tsukuda, T. Ishiyama, J. Nishii, T. Yamashita, H. Kawazoe and T. Omata, *J. Mater. Chem. A*, 2018, **6**, 23628–23637.

S2 T. Shiraiwa, T. Yamasaki, K. Kushimoto, J. Kano and T. Omata, *J. Am. Chem. Soc.*, 2025, **147**, 30757–30767.